

# Characteristic model based all-coefficient adaptive control of an AMB suspended energy storage flywheel test rig

Xujun LYU<sup>1,2</sup>, Long DI<sup>3</sup>, Zongli LIN<sup>4\*</sup>, Yefa HU<sup>1,2</sup> & Huachun WU<sup>1,2</sup>

<sup>1</sup>*School of Mechanical and Electronic Engineering, Wuhan University of Technology, Wuhan 430070, China;*

<sup>2</sup>*Hubei Provincial Engineering Technology Research Center for Magnetic Suspension, Wuhan 430070, China;*

<sup>3</sup>*ASML-HMI, 1762 Automation Pkwy, San Jose CA 95131, USA;*

<sup>4</sup>*Charles L. Brown Department of Electrical and Computer Engineering, University of Virginia, Charlottesville VA 22904-4743, USA*

Received 9 November 2017/Revised 28 December 2017/Accepted 2 January 2018/Published online 10 October 2018

**Abstract** Feedback control of active magnetic bearing (AMB) suspended energy storage flywheel systems is critical in the operation of the systems and has been well studied. Both the classical proportional-integral-derivative (PID) control design method and modern control theory, such as  $H_\infty$  control and  $\mu$ -synthesis, have been explored. PID control is easy to implement but is not effective in handling complex rotordynamics. Modern control design methods usually require a plant model and an accurate characterization of the uncertainties. In each case, few experimental validation results on the closed-loop performance are available because of the costs and the technical challenges associated with the construction of experimental test rigs. In this paper, we apply the characteristic model based all-coefficient adaptive control (ACAC) design method for the stabilization of an AMB suspended flywheel test rig we recently constructed. Both simulation and experimental results demonstrate strong closed-loop performance in spite of the simplicity of the control design and implementation.

**Keywords** adaptive control, characteristic modeling, energy storage flywheels, active magnetic bearings

**Citation** Lyu X J, Di L, Lin Z L, et al. Characteristic model based all-coefficient adaptive control of an AMB suspended energy storage flywheel test rig. *Sci China Inf Sci*, 2018, 61(11): 112204, <https://doi.org/10.1007/s11432-017-9327-0>

## 1 Introduction

Energy storage flywheels are environmentally friendly and have many appealing features, such as high power density, high energy efficiency, short recharge times, wide operating temperature ranges and long life cycles [1–3]. They have found applications in pulse power supplies for linear induction launchers, energy storage devices for grid frequency regulation, power leveling, voltage sag mitigation, uninterruptible power supplies, and hybrid configuration with other types of energy storage devices, and have also been used as gyroscopes for simultaneous attitude control and energy storage in space applications [4, 5].

Flywheels store kinetic energy in a high-speed rotating disk and release the stored energy to the load when it is needed [6]. The energy stored in a flywheel is related to the moment of inertia and is proportional to the square of the rotational speed [7]. The stored energy drastically increases as the increase of the rotational speed. However, mechanical bearings, which suffer from their drawbacks

\* Corresponding author (email: [zl5y@virginia.edu](mailto:zl5y@virginia.edu))

such as friction, vulnerability to wearing, high losses and short lifetime, are often not able to meet the requirements of durable high-speed flywheels. Active magnetic bearings (AMBs), with their merits of no friction, no wear, no lubrication, low losses, fast response, adjustable support magnetic forces and long lifetime [8], make high speed operation of flywheels possible and are thus the ideal support for high-speed flywheel rotors. The AMBs however require control systems, which have turned out to be quite sophisticated for energy storage flywheels [9,10].

A flywheel suspended on AMBs constitutes a complex system including a rotor, flywheel disks, active magnetic bearings, auxiliary bearings, a motor/generator, control systems and energy conversion systems [11,12]. The complexity of AMB suspended flywheel systems often makes the construction of their test rigs too costly in a research laboratory. The absence of past operational data makes the implementation of flywheel AMB system feedback control designs more difficult [13]. For these reasons, we recently developed an experimental platform for AMB suspended energy storage flywheel. This platform was aimed to assist the analysis and control design and was developed on the basis of a flexible rotor-AMB test rig previously constructed in the Rotating Machinery and Controls (ROMAC) Laboratory, University of Virginia [14]. By utilizing the two additional AMBs on the test rig, the platform emulates an equivalent rotordynamic characteristics of an energy storage flywheel, and thus serves as a realistic AMB suspended energy storage flywheel test rig to study the feedback control design on. In this paper, we carry out and implement a control design for AMB suspended flywheel AMB systems on this test rig.

Control design for flywheel AMB systems is an essential problem that has received much attention in the literature. Ahrens et al. [15] analyzed linear quadratic regulator (LQR), decentralized control, and cross feedback control of a high-power energy storage flywheel that is magnetically suspended, and showed by experimental results that instability cannot be avoided but occurs at a much higher rotational speed with cross feedback control than with the first two control methods. Dever et al. [11] designed a control system consisting of five PD controllers with notch filters, which achieved levitation and low speed operation on the NASA Glenn D1 flywheel module. Brown et al. [12] successfully attempted to control only the gyroscopic modes, ignoring the flexible modes, of the NASA Glenn D1 flywheel module for low speed operation by using the cross-axis proportional gains with high- and low-pass filters. Hawkins et al. [16] utilized the gain-scheduling technique to design a MIMO digital control algorithm, which accesses up to four different sets of filter coefficients and gains in different rotor spin speed ranges, for an energy storage flywheel suspended on a five axis AMB system. Peng et al. [17] adopted the small gain theorem to develop a synchronous micro-vibration suppression scheme that reduces the frequency-varying synchronous micro-vibration forces in a flywheel suspended magnetically. These control laws of flywheel AMB systems are based on the classical control theory, which is easy to implement but sometimes fails to handle the complex system rotordynamics or to achieve the desired robust performance.

Modern control theory provides an alternative approach to control design for flywheel AMB systems. Sivrioglu et al. [18] proposed an  $H_\infty$  controller for a zero bias AMB system and verified by experiments its low power consumption in comparison with PID control. Li [10] established a systematic procedure for multivariable robust control synthesis such as gain-scheduled,  $H_\infty$  and  $\mu$ -synthesis of rotor-AMB systems, which was successfully applied in rigid rotors, flexible rotors and gyroscopic rotors. Mushi et al. [19] applied  $\mu$ -synthesis control method on a flexible rotor suspended on AMBs. These modern control designs achieve relatively more robust performance, but entail a plant model and an accurate characterization of the uncertainties. Moreover, the implementation of the resulting controllers requires large amount of on-line computation because of their relatively higher orders. We note that the gyroscopic effects associated with the two AMB test rigs in [10,19] are relatively small. The presence of large disks induces large gyroscopic effects and makes AMB suspended energy storage flywheels even harder to control. In this paper, we apply the characteristic model based all-coefficient adaptive control (ACAC) to AMB suspended energy storage flywheel systems.

Characteristic model based ACAC, originally proposed by Wu et al. [20,21], has found many successful applications in astronautics and other industries. Examples of such applications include the X-34 reusable launch vehicle in its climbing phase [22], automatic train control systems [23], and robotic manipulators [24]. Theoretical investigation of this type of controller design can be found in [25–27]. Di

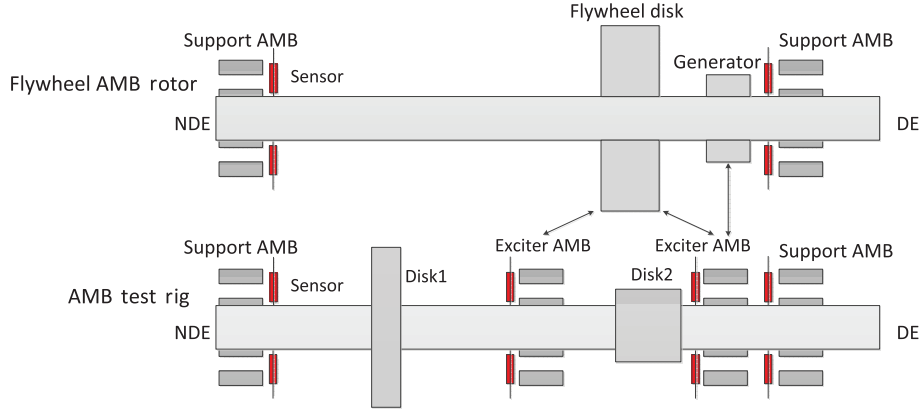


**Figure 1** (Color online) A schematic of the AMB suspended flywheel test rig.

et al. [28] explored the application of characteristic model based ACAC to a flexible rotor-AMB system, which resulted in lower levels of vibration compared with a benchmark  $\mu$ -synthesis controller.

In this paper, we apply the characteristic model based ACAC to the AMB suspended energy storage flywheel platform developed in [14]. Our control objective is to achieve stable operation of the flywheel platform in the presence of large gyroscopic effects and to reduce the level of vibration as much as possible. Both simulation and experimental results verify the effectiveness of our control design in reducing the levels of vibration of the flywheel system. These results not only provide an avenue to solving a challenging control problem associated with AMB suspended energy storage flywheel systems but also help to further demonstrate the promises of the emerging characteristic model based ACAC design method.

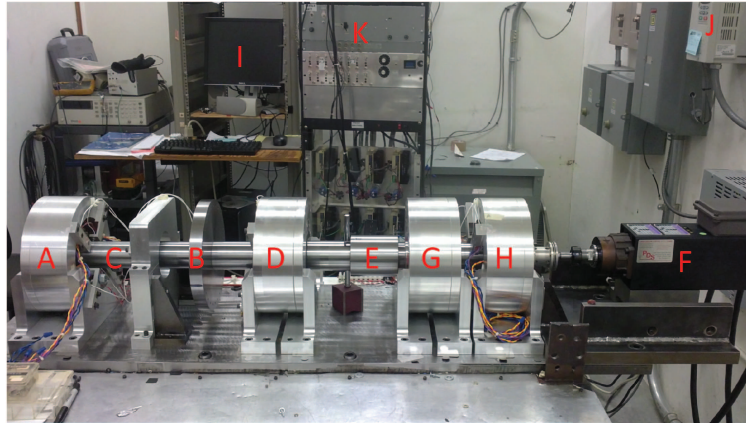
The remainder of this paper is organized as follows. Section 2 describes the AMB suspended flywheel test rig on which we test our control design. Section 3 briefly describes the characteristic model based ACAC design method. Section 4 contains the simulation and experimental results. Section 5 concludes the paper.

## 2 The AMB suspended flywheel test rig

In [14], we proposed to emulate the operation of an energy storage flywheel on a flexible rotor-AMB test rig that was previously constructed and developed an economical and effective platform that serves as a test rig for flywheel control designs. The test rig contains four radial AMBs. The two AMBs at the non-driven end (NDE) and the driven end (DE) of the rotor serve as support AMBs. The two AMBs at the mid span and the quarter span from the driven end of the rotor serve as exciter AMBs. The two main features of a flywheel rotor suspended on AMBs are the coupling between the flywheel shaft and the generator, which is represented as negative stiffness, and the strong gyroscopic effect incurred by the disk [2]. In our platform, we use the exciter AMB at the quarter span to emulate the negative stiffness induced by the generator and both exciter AMBs to generate gyroscopic coupling resulting from the flywheel disk as shown in Figure 1.

### 2.1 The flexible rotor-AMB test rig

The flexible rotor-AMB test rig, shown in Figure 2, was originally designed and constructed in ROMAC [19]. The mechanical part of the test rig contains a flexible rotor, which is 1.23 m long and weights 44.9 kg, and four laminated steel journals that are mounted on the rotor for the four radial AMBs. The test rig also contains two auxiliary ball bearings mounted at the locations of the two support AMBs to prevent damage to the AMBs in the event of a rotor drop. The rotor is driven by a 3.7 kW motor with a variable frequency drive, Colombo RS-90/2, to speeds up to 18000 r/min. A custom shaft extension connects the drive to a flexible disk coupling (Rexnord 75CC140140).



A: Non-driven end support AMB      B: Gyroscopic disk 1      C: Rotor shaft  
 D: Mid-span disturbance AMB      E: Gyroscopic disk 2      F: Electric motor  
 G: Quarter-span disturbance AMB      H: Driven end support AMB      I: Control station  
 J: Variable frequency drive      K: Amplifiers & sensor conditioning station

**Figure 2** (Color online) A photograph of the ROMAC flexible rotor-AMB test rig.

The digital control system is to be implemented on an Innovative Integration M6713 PCI board with a TI C6713B 32-bit floating point DSP chip. The sampling frequency is 12 kHz. Sixteen input-output analog channels that link the 16 sensors to the 16 actuators of the four AMBs are sampled simultaneously. Each AMB is driven by a Copley Controls PWM amplifier, which operates from a 150 V DC power supply with a continuous current rating of 10 A to provide a maximum static load of 1450 N. The rotor position at the location of each support AMB is measured by a Kaman 1 H/15 N eddy current probe and an anti-alias filter circuit attenuates the measurement noise. The rotor motion at the location of each exciter AMB is measured by a Bently Nevada 7200 Series eddy current probe, whose output voltage is changed from  $-10$  to  $0$  V by a gain and offset circuit.

## 2.2 Emulation of an AMB suspended flywheel

The rotor motion of in the test rig is described by

$$M\ddot{q} + (C + \Omega G)\dot{q} + Kq = F_{\text{mag}} + F_{\text{ext}}, \quad (1)$$

where matrices  $M$ ,  $C$  and  $K$ , all symmetric, are respectively the rotor mass matrix, the damping matrix and the stiffness matrix,  $G$  is the gyroscopic effect matrix and is skew-symmetric,  $\Omega$  is the rotational speed,  $F_{\text{mag}}$  is the forces from the support AMBs,  $F_{\text{ext}}$  is the external forces from the exciter AMBs, and  $q$  is the generalized displacement vector.

The following results on the emulation of an AMB suspended flywheel on the ROMAC flexible rotor-AMB test rig are recalled from [14].

### 2.2.1 Analysis and results of the generator effect

Kascak et al. [29] calculated the value of negative stiffness to be about  $9.76 \times 10^4$  N/m for small displacements from the center caused by a permanent magnet motor-generator. This generator induced negative stiffness can be equivalently produced by the exciter AMB located at the quarter span. Simulation results indicate that the rotor  $x$  and  $y$  axis displacements at the four AMBs, in the absence and in the presence of the generator negative stiffness, are almost the same. The maximum rotor displacement at the location of the quarter-span exciter AMB is less than  $2 \times 10^{-5}$  m in both cases. This means that the effect caused by the generator is minimal and negligible. As a result, we do not need to consider this effect of the generator in our study.

**Table 1** Properties of the Exciter AMBs

Property	Mid span/quarter span	Unit
Current gain, $K_{i1}/K_{i2}$	94/91	N/A
Negative stiffness, $K_{x1}/K_{x2}$	165/186	kN/m
Distance between mid and quarter span AMBs, $L$	0.31115	m

### 2.2.2 Analysis and results of gyroscopic effect of the flywheel disk

The two exciter AMBs (see Figure 2) are used to generate the gyroscopic moments that mimic those that would be generated by a flywheel disk located between the two exciter AMBs, as shown in Figure 1. In particular, the forces of the exciter AMBs are generated to be equal to the gyroscopic forces that would be generated by the flywheel disk according to the following equations:

$$i_{px1} = \frac{K_{x1}}{K_{i1}}x_1 + \frac{J_t}{K_{i1}L^2}(\ddot{x}_2 - \ddot{x}_1) - \frac{J_p\Omega}{K_{i1}L^2}(\dot{y}_2 - \dot{y}_1), \quad (2)$$

$$i_{px2} = \frac{K_{x2}}{K_{i2}}x_2 - \frac{J_t}{K_{i2}L^2}(\ddot{x}_2 - \ddot{x}_1) + \frac{J_p\Omega}{K_{i2}L^2}(\dot{y}_2 - \dot{y}_1), \quad (3)$$

$$i_{py1} = \frac{K_{x1}}{K_{i1}}y_1 - \frac{J_t}{K_{i1}L^2}(\ddot{y}_2 - \ddot{y}_1) - \frac{J_p\Omega}{K_{i1}L^2}(\dot{x}_2 - \dot{x}_1), \quad (4)$$

$$i_{py2} = \frac{K_{x2}}{K_{i2}}y_2 + \frac{J_t}{K_{i2}L^2}(\ddot{y}_2 - \ddot{y}_1) + \frac{J_p\Omega}{K_{i2}L^2}(\dot{x}_2 - \dot{x}_1), \quad (5)$$

where  $i_{px1}$ ,  $i_{px2}$ ,  $i_{py1}$  and  $i_{py2}$  are respectively the perturbation currents of the two exciter AMBs in the  $x$  and  $y$  directions,  $K_{i1}$ ,  $K_{i2}$ ,  $K_{x1}$  and  $K_{x2}$  are respectively the current gains and the negative stiffnesses of the two exciter AMBs in the  $x$  and  $y$  directions,  $x_1$ ,  $x_2$ ,  $y_1$  and  $y_2$  are respectively rotor displacements at the locations of the two exciter AMBs in the  $x$  and  $y$  directions,  $L$  is the distance between the two exciter AMBs,  $J_p$  is the polar moment of inertia of the flywheel disk,  $J_t$  is the transverse moment of inertia of the flywheel disk, and  $\Omega$  is the rotational speed. For the ROMAC flexible-rotor AMB test rig shown in Figure 2, the properties of the two exciter AMBs are listed in Table 1.

We simulated a flywheel disk with the polar moment of inertia  $J_p = 0.042 \text{ kg}\cdot\text{m}^2$  and the transverse moment of inertia  $J_t = 0.021 \text{ kg}\cdot\text{m}^2$ . We simulated both the gyroscopic forces caused by the original gyroscopic matrix  $G$  resulting from Disk 1 and the forces generated by the two exciter AMBs as an emulator of a disk. The results are shown in Figures 3 and 4, respectively. The similar patterns in the actual and emulated gyroscopic forces indicate the feasibility of the emulation approach.

We also simulated the rotor orbits under the influence of the excitation forces of different magnitudes and the gyroscopic forces due to different scales of the gyroscopic matrix  $G$  at the rotational speed 7600 r/min. The results are shown in Figures 5 and 6. In these figures,  $dnx$  and  $dny$  denote respectively the rotor displacements in the  $x$  and  $y$  axes at the location of the non-driven end AMB,  $dmx$  and  $dmy$  denote respectively the rotor displacements in the  $x$  and  $y$  axes at the location of the mid span exciter AMB,  $dqx$  and  $dqy$  denote respectively the rotor displacements in the  $x$  and  $y$  axes at the location of the quarter span exciter AMB, and  $ddx$  and  $ddy$  denote respectively the rotor displacements in the  $x$  and  $y$  axes at the location of the driven end AMB. As is clear in Figure 5, the orbits tilt counterclockwise at the locations of the support AMBs as additional gyroscopic forces are increased by adding a higher percentage of the original gyroscopic matrix  $G$ . This tilting phenomenon resembles what displays in Figure 6, where the rotor orbits tilt counterclockwise at the locations of the two support AMBs as excitation forces of different magnitudes are applied.

In the experiments, the two exciter AMBs generate the required excitation forces in opposite directions. Shown in Figures 7 and 8 are the rotor displacement measurements at the locations of the two support AMBs and the two exciter AMBs, with  $J_p = 0.021 \text{ kg}\cdot\text{m}^2$  and  $\Omega = 7600 \text{ r/min}$ . The exciter AMBs are turned on at around 33.1 s. A comparison of the rotor orbits in the absence and in the presence of the excitation forces is shown in Figures 9 and 10. The maximum amplitudes of the orbits at the locations of the two support AMBs are both around  $5 \times 10^{-5} \text{ m}$  at the rotational speed 7600 r/min, and the rotor tilts counterclockwise, resembling what the simulation results show in Figure 6.

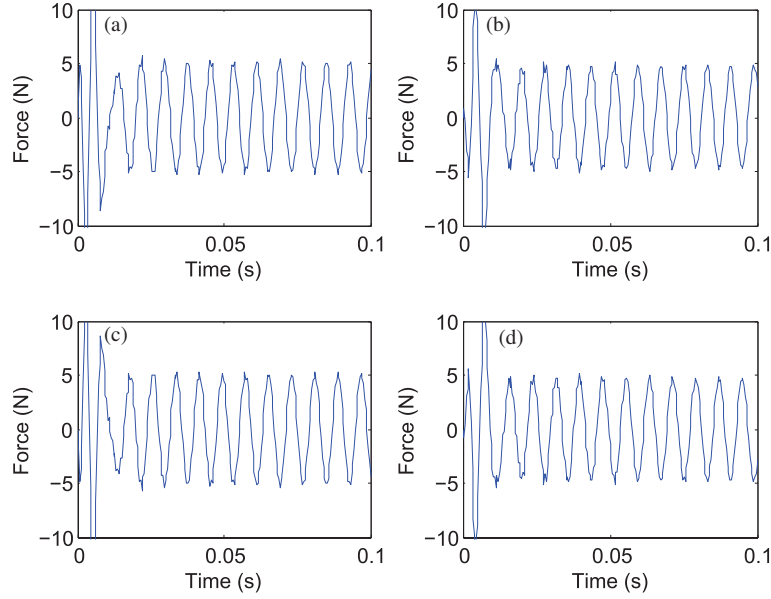


**Figure 3** (Color online) Emulated gyroscopic forces generated by the exciter AMBs at the mid span ((a) F\_Midx and (b) F\_Midy) and at the quarter span ((c) F\_Quax and (d) F\_Quay) at  $\Omega = 7600$  r/min.

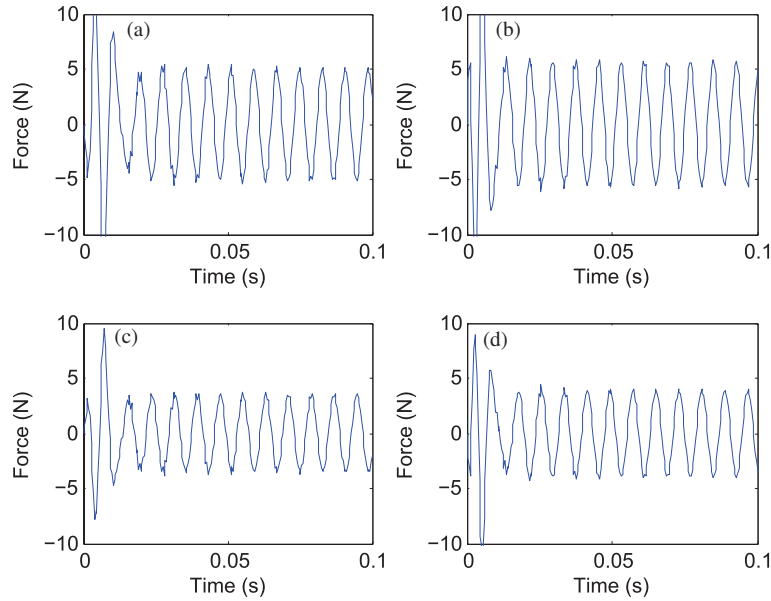


**Figure 4** (Color online) Actual forces caused by the gyroscopic matrix  $G$  at the non-driven end ((a) FG\_dnx and (b) FG\_dny) and at the driven end support AMB ((a) FG\_ddx and (b) FG\_ddy) at  $\Omega = 7600$  r/min.

To sum up, we emulated the operation of an energy storage flywheel on the ROMAC flexible rotor-AMB test rig with two exciter AMBs. Experimental results verified the simulation results. As a result, we provide a low cost but effective test rig to study the behaviors of energy storage flywheels and the control design for them. In this paper, we develop and implement a control design for this AMB suspended flywheel test rig.

### 3 Characteristic model based all-coefficient adaptive control

The basic idea of characteristic modeling is that a higher order system can be represented equivalently as a lower order, often the 1st and 2nd order, time-varying linear system, which, when the sampling period

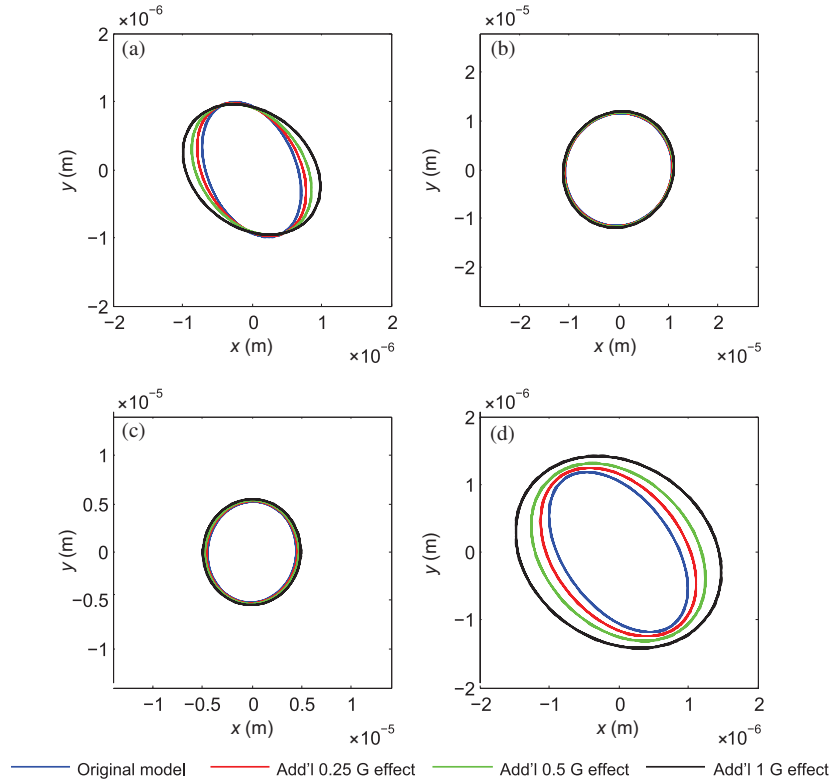


**Figure 5** (Color online) Rotor orbits under different additional gyroscopic forces of different scales of  $G$  ( $\Omega = 7600$  r/min). (a)  $dnx-dny$ ; (b)  $dmx-dmy$ ; (c)  $dqx-dqy$ ; (d)  $ddx-ddy$ .

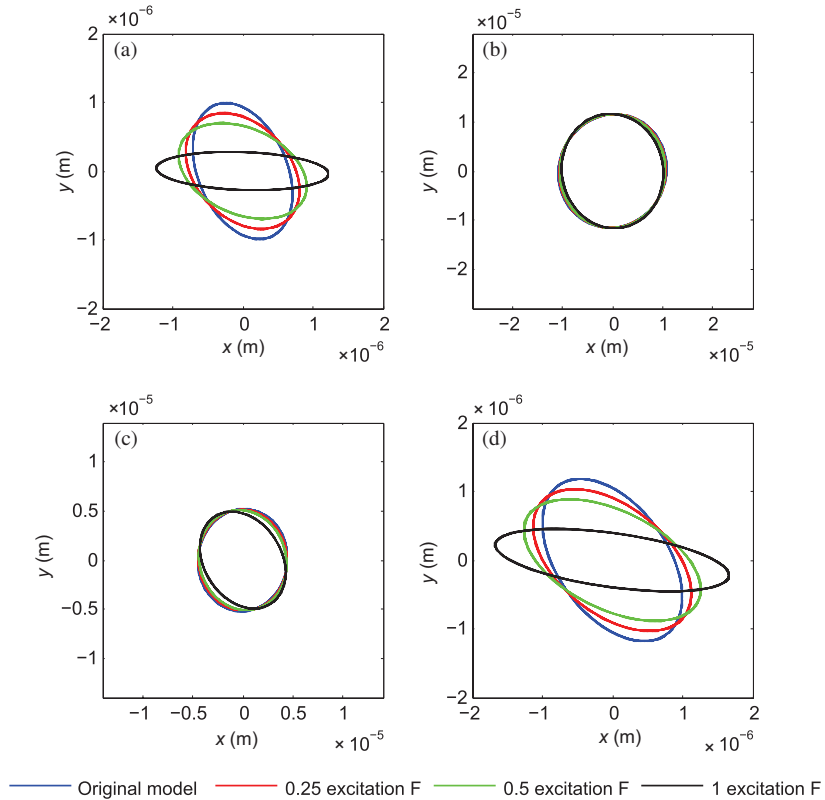


**Figure 6** (Color online) Rotor orbits under excitation forces of different magnitudes ( $\Omega = 7600$  r/min). (a)  $dnx-dny$ ; (b)  $dmx-dmy$ ; (c)  $dqx-dqy$ ; (d)  $ddx-ddy$ .

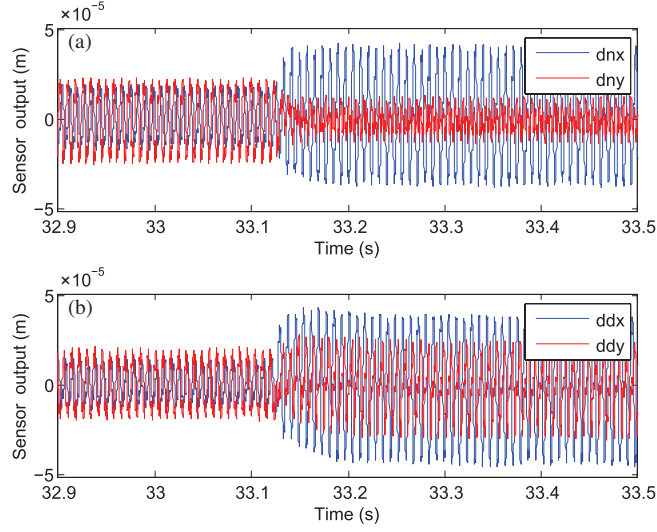


**Figure 7** (Color online) Experimental results with  $J_p = 0.021 \text{ kg}\cdot\text{m}^2$  and  $\Omega = 7600 \text{ r/min}$ : sensor measurements at the locations of the support AMBs. (a) dnx, dny; (b) ddx, ddy.

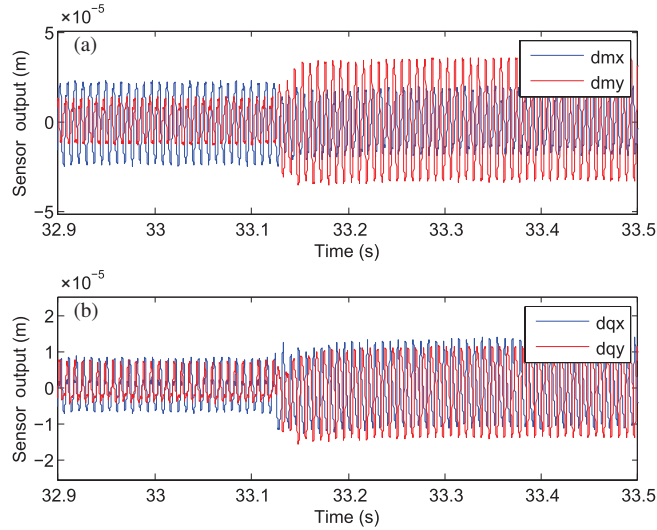


**Figure 8** (Color online) Experimental results with  $J_p = 0.021 \text{ kg}\cdot\text{m}^2$  and  $\Omega = 7600 \text{ r/min}$ : sensor measurements at the locations of the exciter AMBs. (a) dm x, dm y; (b) dq x, dq y.

is sufficiently small, has the same output as the original system at the sampling instants. This lower order system is called the characteristic model of the original system [20, 21]. The time-varying coefficients of the characteristic model, referred to as the characteristic parameters, are then identified online adaptively. Based on the characteristic model, a simple PID type control law is designed. The resulting feedback law is referred to as the characteristic model based all-coefficient adaptive control (ACAC) law. A schematic diagram of the characteristic model based ACAC system is depicted in Figure 11.

### 3.1 Characteristic modeling

Let a linear time-invariant system be described by the transfer function:

$$G(s) = \frac{b_m s^m + b_{m-1} s^{m-1} + \dots + b_1 s + b_0}{s^n + a_{n-1} s^{n-1} + \dots + a_1 s + a_0}, \quad (6)$$

where  $a_i$ 's and  $b_i$ 's are constant parameters of the plant. It has been established in [20, 21] that, if the control objective is position keeping or reference tracking and the sampling period  $T$  is sufficiently small,

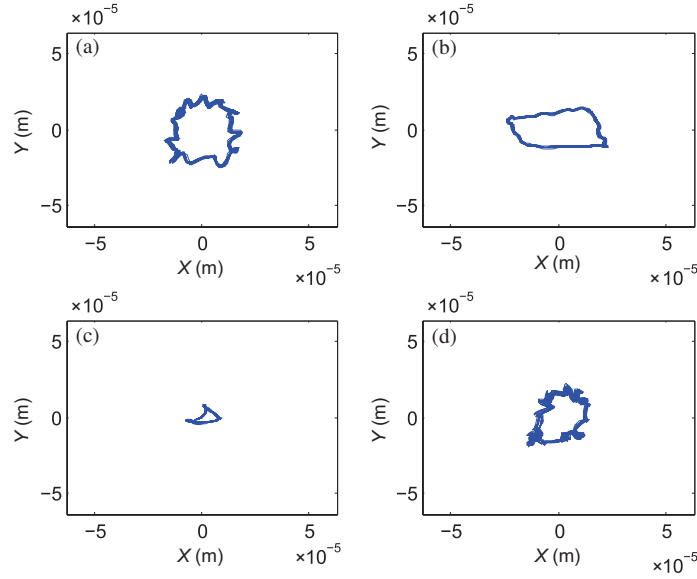


**Figure 9** (Color online) Experimental rotor orbits in the absence of excitation forces when  $\Omega = 7600$  r/min. (a) dnx-dny; (b) dmx-dmy; (c) dqx-dqy; (d) ddx-ddy.

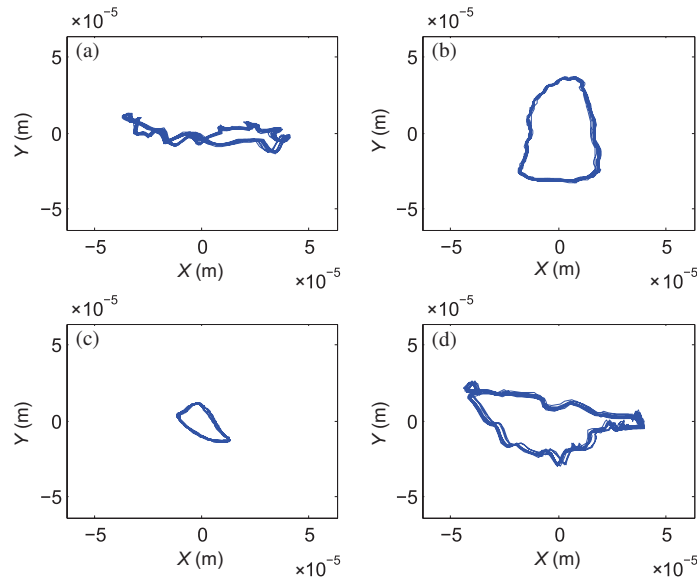


**Figure 10** (Color online) Experimental rotor orbits in the presence of excitation forces when  $J_p = 0.021$  kg·m<sup>2</sup> and  $\Omega = 7600$  r/min. (a) dnx-dny; (b) dmx-dmy; (c) dqx-dqy; (d) ddx-ddy.

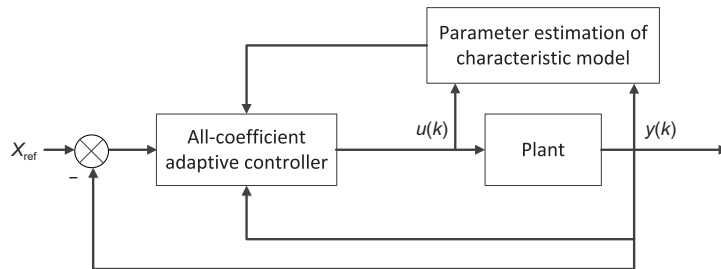


**Figure 11** A diagram of the characteristic model based ACAC system.

the characteristic model takes the following form:

$$y(k) = f_1(k)y(k-1) + f_2(k)y(k-2) + g_0(k)u(k-1) + g_1(k)u(k-2), \quad (7)$$

where  $u(k)$  is the control input,  $y(k)$  is the system output, and  $f_1(k)$ ,  $f_2(k)$ ,  $g_0(k)$  and  $g_1(k)$  are the characteristic parameters. Despite its simplicity, the characteristic model produces the same output as the original model (6) at each sampling instant. Characteristic modeling is different from the conventional model reduction methods in that it compresses the plant information into the time-varying coefficients instead of truncating parts of the plant model.

To present the identification algorithm for the characteristic parameters, we rewrite (7) in a compact form:

$$y(k) = \varphi^T(k)\theta(k),$$

where

$$\begin{aligned} \varphi(k) &= [y(k-1) \ y(k-2) \ u(k-1) \ u(k-2)]^T, \\ \theta(k) &= [f_1(k) \ f_2(k) \ g_0(k) \ g_1(k)]^T. \end{aligned}$$

Let  $\hat{\theta}(k) = [\hat{f}_1(k) \ \hat{f}_2(k) \ \hat{g}_0(k) \ \hat{g}_1(k)]^T$  be the estimate of vector  $\theta(k)$ . Then, the estimation error of the output is given as

$$\varepsilon(k) = y(k) - \varphi^T(k)\hat{\theta}(k).$$

The characteristic parameters are then identified by the following gradient adaptive law:

$$\begin{aligned} \hat{\theta}_u(k+1) &= \hat{\theta}(k) + \frac{\gamma\varphi(k)\varepsilon(k)}{\delta + \varphi^T(k)\varphi(k)}, \\ \hat{\theta}(k+1) &= \pi(\hat{\theta}_u(k+1)), \end{aligned}$$

where  $\delta \geq 0$ ,  $0 \leq \gamma \leq 2$ , and, for a scalar  $x$ ,  $\pi(x)$  is the projection of  $x$  into the set

$$\mathcal{N} = \{(f_1, f_2) : 1.9844 < f_1 < 2.2663, -1.2840 < f_2 < -1\}.$$

Also, the initial values for  $g_0(k)$  and  $g_1(k)$  are chosen to be positive scalars that are much smaller than one.

### 3.2 Characteristic model based ACAC

The characteristic model based ACAC law takes the following form:

$$u_c(k) = u_O(k) + u_G(k) + u_D(k) + u_I(k), \tag{8}$$

where

- $u_O(k)$  : maintaining/tracking control,
- $u_G(k)$  : golden section adaptive control,
- $u_D(k)$  : differential control,
- $u_I(k)$  : integral control,

and are respectively given by

$$\begin{aligned} u_O(k) &= \frac{y_r(k) - \hat{f}_1(k)y(k) - \hat{f}_2(k)y(k-1) - \hat{g}_1(k)u_O(k-1)}{\hat{g}_0(k) + \lambda_1}, \\ u_G(k) &= \frac{l_1\hat{f}_1(k)\tilde{y}(k) + l_2\hat{f}_2(k)\tilde{y}(k-1) + \hat{g}_1(k)u_G(k-1)}{\hat{g}_0(k) + \lambda_1}, \\ u_D(k) &= d_1 \frac{\tilde{y}(k) - \tilde{y}(k-1)}{T}, \\ u_I(k) &= u_I(k-1) + d_2\tilde{y}(k), \end{aligned}$$

where  $y_r(k)$  is the reference output,  $\lambda_1$  is a positive constant,  $\tilde{y}(k) = y_r(k) - y(k)$ ,  $l_1 = 0.382$ ,  $l_2 = 0.618$ ,  $d_1$  and  $d_2$  are both positive constants.

The stability and performance of the closed-loop system consisting of the characteristic model and the characteristic model based ACAC have been established in [21, 30, 31], and are summarized in the following theorem.

**Theorem 1.** Consider the linear time-invariant system (6). The closed-loop system consisting of the characteristic model (7) and the characteristic model based all-coefficient adaptive controller (8) is asymptotically stable at the origin and its output tracks a constant reference output  $y_r$ .

## 4 Characteristic model based ACAC of the AMB suspended flywheel test rig

In this section, we present our results on the application of the characteristic model based ACAC to the AMB suspended flywheel test rig as described in Section 2. The effectiveness of our control design will be validated both by the simulation results and by the experimental results.

### 4.1 Simulation results

The simulation is performed on a Simulink model of the test rig. This Simulink model is in the state space form with 36 states, 12 inputs and 20 outputs. The 12 inputs include external forces from the exciter AMBs, which emulate the flywheel operation, the unbalance forces, and the control voltages of the two support AMBs. The 20 outputs include the rotor displacements at the locations of the four AMBs and the forces produced by the two support AMBs. The polar moment of inertia of the emulated flywheel is  $J_p = 0.042 \text{ kg}\cdot\text{m}^2$  and the transverse moment of inertia is  $J_t = 0.021 \text{ kg}\cdot\text{m}^2$ . The flywheel emulation on the ROMAC flexible rotor-AMB test rig, as reported in [14], was stabilized by a  $\mu$ -synthesis controller due to the complex dynamics and the presence of strong uncertainties. The rotor orbits representing the emulated flywheel under the  $\mu$ -synthesis controller was shown in Figure 6. We use the black curves in Figure 6, which correspond to the full simulated excitation force  $F$ , for comparison with the rotor orbits under the characteristic model based all-coefficient adaptive controller.

In our simulation study, an identical characteristic model based ACAC law is implemented for each of the four control channels, the  $x$  and  $y$  axes of the two support AMBs, as a substitute for the  $\mu$ -synthesis controller. The initial values for the estimation of the characteristic model are selected as  $f_1(0) = 2.102$ ,  $f_2(0) = -1.104$  and  $g_0(0) = g_1(0) = 0.001$ , and the parameters in the adaptation law are chosen as  $\delta = 3.5$  and  $\gamma = 1.5$  in all channels. The control parameters in all control channels are  $\lambda_1 = 0.2$ ,  $d_1 = 0.02$  and  $d_2 = 10$ .

Shown in Figures 12 and 13 are the rotor displacements at the locations of all four AMBs under the characteristic model based ACAC law at the rotational speed 7600 r/min. Shown in Figure 14 are the simulated rotor orbits (red curves) in comparison with the corresponding orbits (black curves) from Figure 6. It is clear that the displacements in both  $x$  and  $y$  axes at the locations of the two support AMBs are much smaller under the characteristic model based ACAC. The maximum amplitude  $1.2 \times 10^{-6} \text{ m}$  of the orbits represents a 50% reduction in vibration.

### 4.2 Experiment results

Our experiments are carried out on the AMB suspended flywheel test rig described in Section 2 with  $J_p = 0.021 \text{ kg}\cdot\text{m}^2$  and  $\Omega = 7600 \text{ r/min}$ . The characteristic model based ACAC algorithm is converted to a C++ code to replace the  $\mu$ -synthesis control algorithm used in the original AMB suspended flywheel test rig. The initial values for the parameter estimation,  $f_1(0)$ ,  $f_2(0)$ ,  $g_0(0)$  and  $g_1(0)$ , the parameters in the adaptation law,  $\delta$  and  $\gamma$ , and the control parameters,  $\lambda_1$ ,  $d_1$  and  $d_2$  in each control channel, are all set to be the same as those in the simulation.

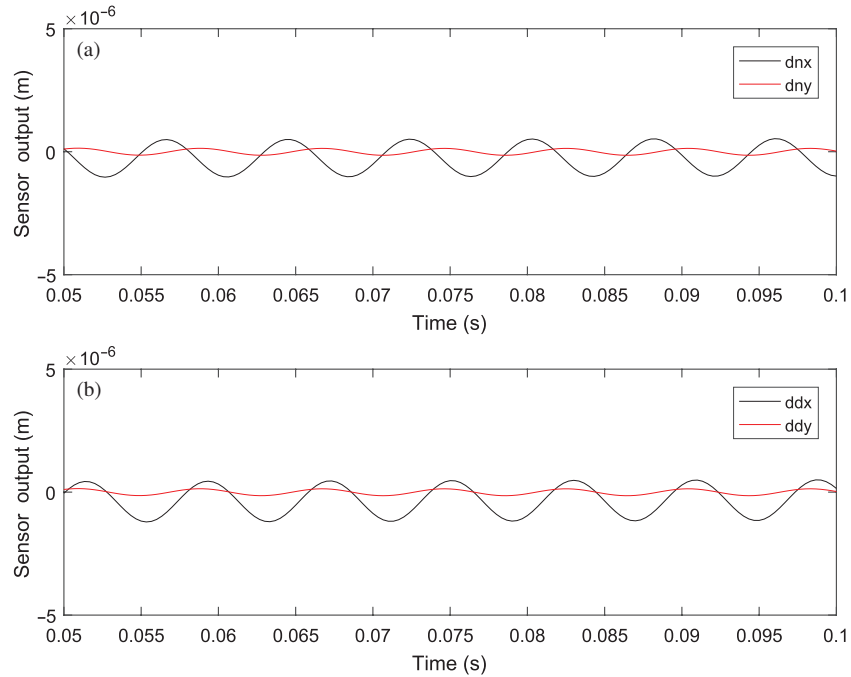


**Figure 12** (Color online) Simulation results with the characteristic model based ACAC law when  $\Omega = 7600$  r/min: sensor measurements at the locations of the two support AMBs. (a) dnx, dny; (b) ddx, ddy.

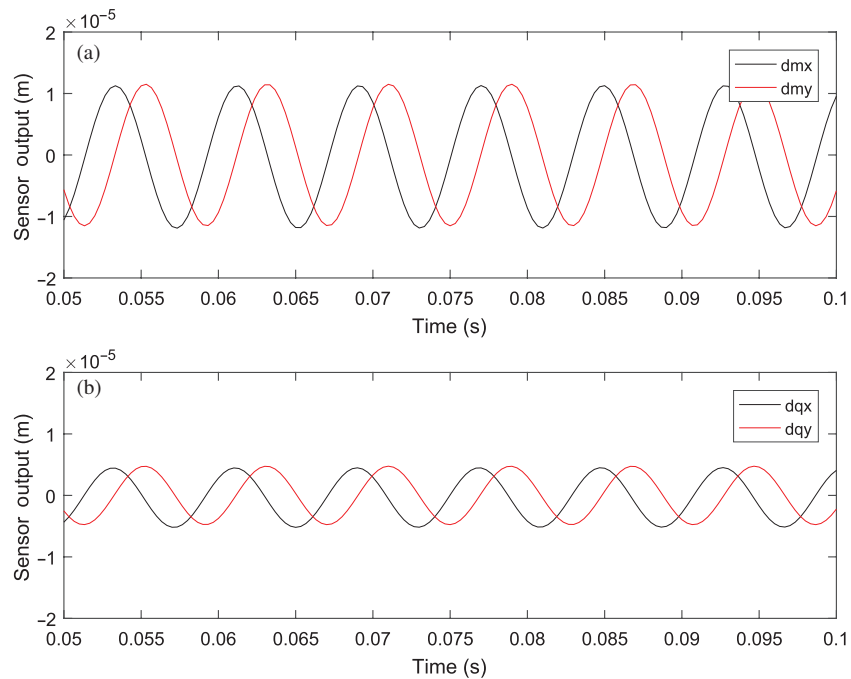


**Figure 13** (Color online) Simulation results with the characteristic model based ACAC law when  $\Omega = 7600$  r/min: sensor measurements at the locations of the two exciter AMBs. (a) dm<sub>x</sub>, dm<sub>y</sub>; (b) dq<sub>x</sub>, dq<sub>y</sub>.

Shown in Figures 15 and 16 are the rotor displacement measurements at the locations of the support and exciter AMBs with the characteristic model based ACAC law. The maximum amplitude of rotor displacements at all these locations is less than  $3 \times 10^{-5}$  m. Shown in Figure 17 in red curves are the rotor orbits under the characteristic model based ACAC law. For comparison, we also show in Figure 17 in blue curves the experimental results under the  $\mu$ -synthesis controller described in Section 2. It is observed that the characteristic model based ACAC design results in smaller rotor orbits at all AMB locations,

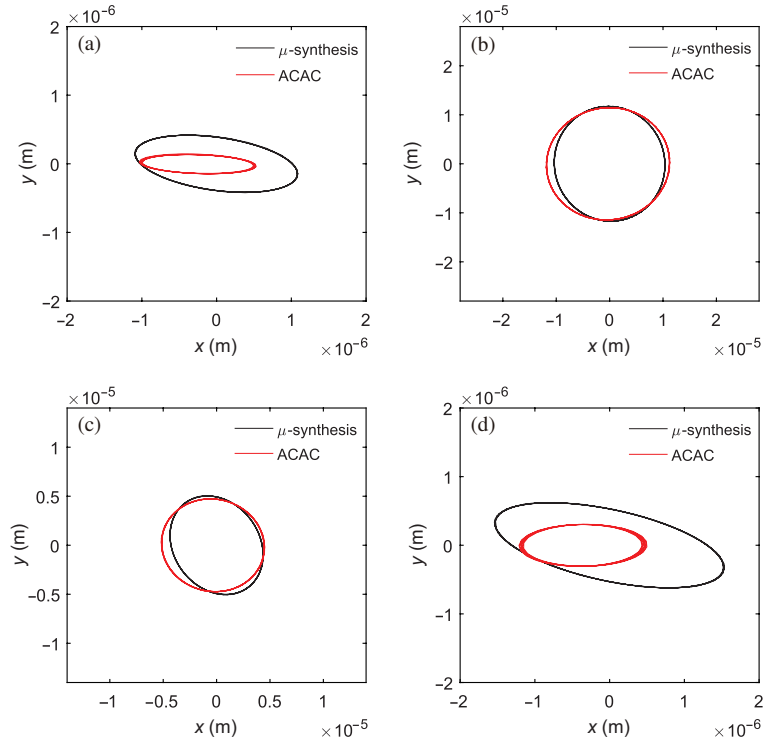


**Figure 14** (Color online) Simulation results of the orbits at  $\Omega = 7600$  r/min: characteristic model based ACAC vs.  $\mu$ -synthesis controller. (a)  $d_{nx}$ - $d_{ny}$ ; (b)  $d_{mX}$ - $d_{mY}$ ; (c)  $d_{qX}$ - $d_{qY}$ ; (d)  $d_{dx}$ - $d_{dy}$ .

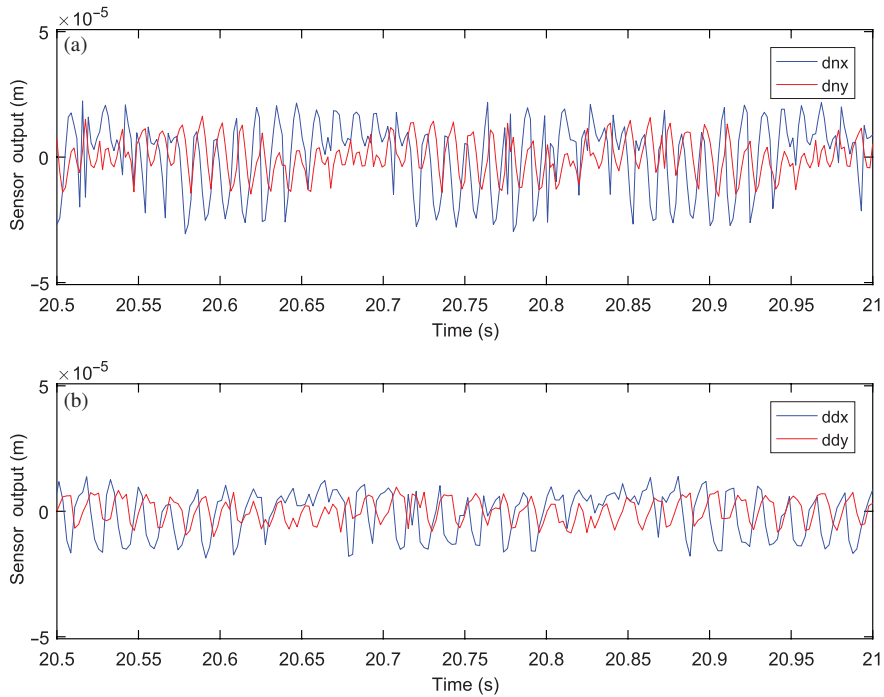


**Figure 15** (Color online) Experimental results with the characteristic model based ACAC law when  $\Omega = 7600$  r/min: sensor measurements at the locations of the two support AMBs. (a)  $d_{nx}$ ,  $d_{ny}$ ; (b)  $d_{dx}$ ,  $d_{dy}$ .

which represent approximately a 50% reduction in vibration at the location of the non-driven end AMB location, a 60% reduction at the locations of the two exciter AMBs, and a 25% reduction at the location of the driven end AMB. These experimental results validate that the characteristic model based ACAC is effective in vibration suppression on the AMB suspended energy storage flywheel test rig.

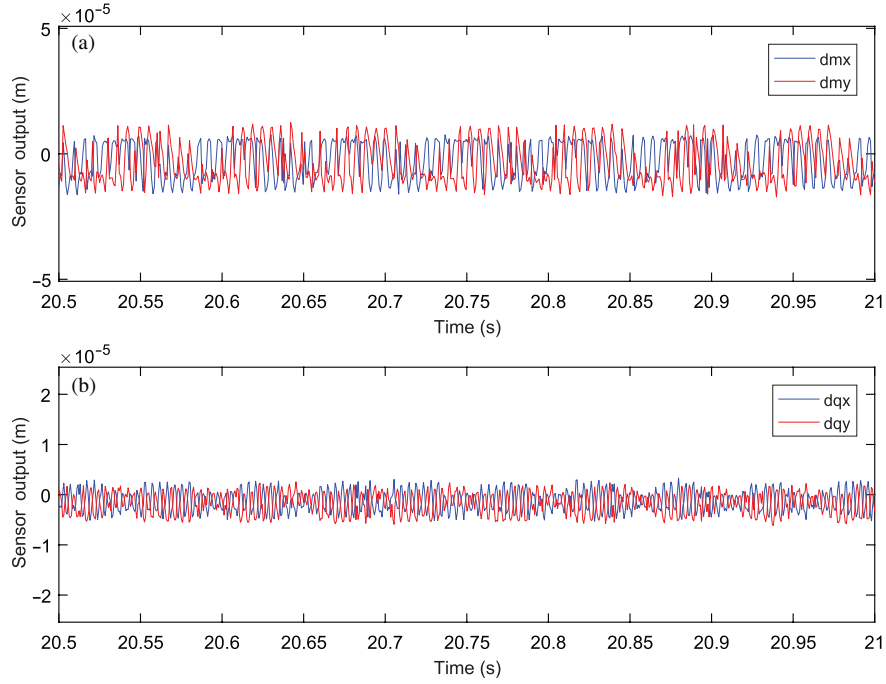


**Figure 16** (Color online) Experimental results with the characteristic model based ACAC law when  $\Omega = 7600$  r/min: sensor measurements at the locations of the two exciter AMBs. (a) dmx, dmy; (b) dqx, dqy.

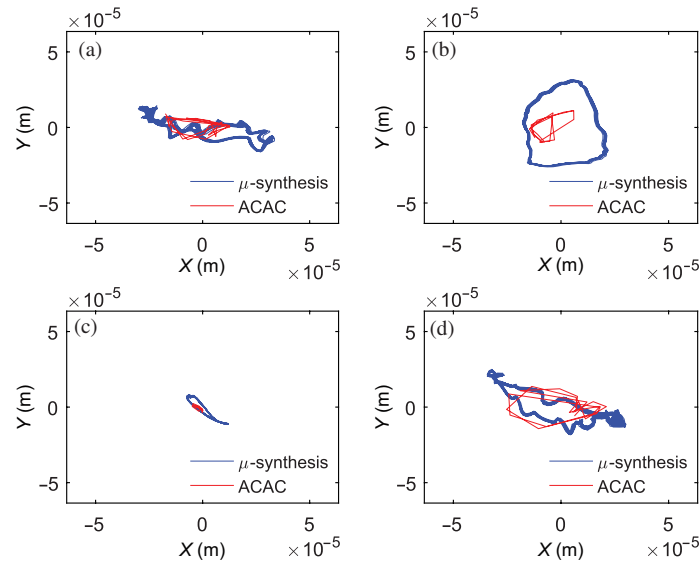


**Figure 17** (Color online) Experimental rotor orbits at  $\Omega = 7600$  r/min: characteristic model based ACAC vs.  $\mu$ -synthesis controller. (a) dnx-dny; (b) dmx-dmy; (c) dqx-dqy; (d) ddx-ddy.

## 5 Conclusion

In this paper, the characteristic model based all-coefficient adaptive control (ACAC) was applied to the AMB suspended energy storage flywheel test rig we have recently developed. The test rig uses the two exciter AMBs along the shaft to emulate the flywheel characteristics, as recalled in Section 2. Characteristic model based ACAC was implemented on the two support AMBs located at two ends of the shaft. Despite its simplicity, the characteristic model based ACAC was shown to be capable of achieving strong control performance by both simulation and experimental results. It suppresses the vibration on the AMB suspended flywheel test rig to a significantly higher level than the originally designed  $\mu$ -synthesis controller could.

## References

- 1 Mousavi G S M, Faraji F, Majazi A, et al. A comprehensive review of flywheel energy storage system technology. *Renew Sustain Energy Rev*, 2017, 67: 477–490
- 2 Hebner R, Beno J, Walls A. Flywheel batteries come around again. *IEEE Spectr*, 2002, 39: 46–51
- 3 Bitterly J G. Flywheel technology: past, present and 21st century projections. *IEEE Aerosp Electron Syst Mag*, 1998, 13: 13–16
- 4 Reid C M, Miller T B, Hoberecht M A, et al. History of electrochemical and energy storage technology development at NASA Glenn Research Center. *J Aerosp Eng*, 2013, 26: 361–371
- 5 Farhadi M, Mohammed O. Energy storage technologies for high-power applications. *IEEE Trans Ind Applicat*, 2016, 52: 1953–1961
- 6 Zhao H, Wu Q, Hu S, et al. Review of energy storage system for wind power integration support. *Appl Energy*, 2015, 137: 545–553
- 7 Hemmati R, Saboori H. Emergence of hybrid energy storage systems in renewable energy and transport applications - A review. *Renew Sustain Energy Rev*, 2016, 65: 11–23
- 8 Schweitzer G, Maslen E H. *Magnetic Bearings: Theory, Design, and Application to Rotating Machinery*. Berlin: Springer, 2009
- 9 Li G, Lin Z, Allaire P E, et al. Modeling of a high speed rotor test rig with active magnetic bearings. *J Vib Acoust*, 2006, 128: 269–281
- 10 Li G. Robust stabilization of rotor-active magnetic bearing systems. Dissertation for Ph.D. Degree. Charlottesville: University of Virginia, 2007
- 11 Dever T P, Brown G V, Duffy K P, et al. Modeling and development of a magnetic bearing controller for a high speed flywheel system. In: *Proceedings of the 2nd International Energy Conversion Engineering Conference*, Providence, 2004. 5626
- 12 Brown G V, Kascak A, Jansen R H, et al. Stabilizing gyroscopic modes in magnetic-bearing-supported flywheels by using cross-axis proportional gains. In: *Proceedings of the AIAA Guidance, Navigation, and Control Conference*, San Francisco, 2005. 5955
- 13 Arghandeh R, Pipattanasomporn M, Rahman S. Flywheel energy storage systems for ride-through applications in a facility microgrid. *IEEE Trans Smart Grid*, 2012, 3: 1955–1962
- 14 Lyu X, Di L, Yoon S Y, et al. A platform for analysis and control design: emulation of energy storage flywheels on a rotor-AMB test rig. *Mechatronics*, 2016, 33: 146–160
- 15 Ahrens M, Kucera L, Larsonneur R. Performance of a magnetically suspended flywheel energy storage device. *IEEE Trans Contr Syst Technol*, 1996, 4: 494–502
- 16 Hawkins L A, Murphy B T, Kajs J. Analysis and testing of a magnetic bearing energy storage flywheel with gain-scheduled, MIMO control. In: *Proceedings of the ASME Turbo Expo*, Munich, 2000. 1–8
- 17 Peng C, Fan Y, Huang Z, et al. Frequency-varying synchronous micro-vibration suppression for a MSFW with application of small-gain theorem. *Mech Syst Signal Process*, 2017, 82: 432–447
- 18 Sivrioglu S, Nonami K, Saigo M. Low power consumption nonlinear control with  $H_\infty$  compensator for a zero-bias flywheel AMB system. *J Vib Control*, 2004, 10: 1151–1166
- 19 Mushi S E, Lin Z, Allaire P E. Design, construction, and modeling of a flexible rotor active magnetic bearing test rig. *IEEE/ASME Trans Mechatron*, 2012, 17: 1170–1182
- 20 Wu H, Hu J, Xie Y. Characteristic model-based all-coefficient adaptive control method and its applications. *IEEE Trans Syst Man Cybern Part C-Appl Rev*, 2007, 37: 213–221
- 21 Wu H, Hu J, Xie Y, et al. *Characteristic Model-Based Intelligent Adaptive Control* (in Chinese). Beijing: China Science and Technology Press, 2009
- 22 Meng B, Wu H X, Lin Z L. Characteristic model based control of the X-34 reusable launch vehicle in its climbing phase. *Sci China Ser F-Inf Sci*, 2009, 52: 2216–2225
- 23 Gao S G, Dong H R, Ning B. Characteristic model-based all-coefficient adaptive control for automatic train control systems. *Sci China Inf Sci*, 2014, 57: 092201
- 24 Wang L J, Meng B. Characteristic model-based control of robotic manipulators with dynamic uncertainties. *Sci China Inf Sci*, 2017, 60: 079201
- 25 Huang J F, Kang Y, Meng B, et al. Characteristic model based adaptive controller design and analysis for a class of SISO systems. *Sci China Inf Sci*, 2016, 59: 052202
- 26 Jiang T T, Wu H X. A framework for stability analysis of high-order nonlinear systems based on the CMAC method. *Sci China Inf Sci*, 2016, 59: 112201
- 27 Sun D Q. Stability analysis of golden-section adaptive control systems based on the characteristic model. *Sci China Inf Sci*, 2017, 60: 092205
- 28 Di L, Lin Z. Control of a flexible rotor active magnetic bearing test rig: a characteristic model based all-coefficient adaptive control approach. *Control Theor Technol*, 2014, 12: 1–12
- 29 Kascak P E, Dever T P, Jansen R H. Magnetic circuit model of PM motor-generator to predict radial forces. In: *Proceedings of the 1st International Energy Conversion Engineering Conference*, Cleveland, 2003
- 30 Xie Y, Wu H. The application of the golden section in adaptive robust controller design (in Chinese). *Acta Autom Sin*, 1992, 18: 178–185
- 31 Wu H, Hu J, Xie Y, et al. Theory and applications of characteristic modeling: an introductory overview. *Int J Intell Contr Syst*, 2015, 20: 1–8